Bridging the N-terminal and middle domains in FliG of the flagellar rotor

Dagnija Tupiņa [a,b], Alexander Krah [a], Jan K. Marzinek [a], Lorena Zuzic [a,c], Adam A. Moverley [d], Chrystala Constantinidou [b], Peter J. Bond [a,e,*]

[a] *Bioinformatics Institute, A*STAR, 30 Biopolis Street, 138671, Singapore*
[b] *Warwick Medical School, University of Warwick, Coventry, CV4 7AL, United Kingdom*
[c] *Department of Chemistry, Faculty of Science and Engineering, Manchester Institute of Biotechnology, The University of Manchester, Manchester, M1 7DN, United Kingdom*
[d] *Department of Cell and Developmental Biology, University College London, London, WC1E 6BT, United Kingdom*
[e] *Department of Biological Sciences, National University of Singapore, 14 Science Drive 4, 117543, Singapore*

ARTICLE INFO

Handling Editor: Natalie Strynadka

ABSTRACT

Flagella are necessary for bacterial movement and contribute to various aspects of virulence. They are complex cylindrical structures built of multiple molecular rings with self-assembly properties. The flagellar rotor is composed of the MS-ring and the C-ring. The FliG protein of the C-ring is central to flagellar assembly and function due to its roles in linking the C-ring with the MS-ring and in torque transmission from stator to rotor. No high-resolution structure of an assembled C-ring has been resolved to date, and the conformation adopted by FliG within the ring is unclear due to variations in available crystallographic data. Here, we use molecular dynamics (MD) simulations to study the conformation and dynamics of FliG in different states of assembly, including both in physiologically relevant and crystallographic lattice environments. We conclude that the linker between the FliG N-terminal and middle domain likely adopts an extended helical conformation in vivo, in contrast with the contracted conformation observed in some previous X-ray studies. We further support our findings with integrative model building of full-length FliG and a FliG ring model that is compatible with cryo-electron tomography (cryo-ET) and electron microscopy (EM) densities of the C-ring. Collectively, our study contributes to a better mechanistic understanding of the flagellar rotor assembly and its function.

1. Introduction

Many bacteria have one or more flagella that enable their biased movement within the environment. Flagella contribute to bacterial virulence and their ability to colonize the host via motility, linked with chemotaxis, as well as via involvement in adhesion to target surfaces, biofilm formation and secretion of virulence factors (Chaban et al., 2015). The composition and structure of the flagellar complex has been studied for many years, yet numerous details still remain to be clarified about this intricate multi-component structure.

While the overall flagellar structure and component proteins are known, the configurations and positions of individual domains and are still being investigated (Chevance and Hughes, 2008). To fully understand the mechanisms governing this molecular engine, it is crucial to elucidate individual structures, their conformational dynamics, as well as the nature of the interactions between them (Minamino and Imada, 2015). The flagellum consists of a propeller, a joint, and a rotor

(Terashima et al., 2008). The rotor associates with stators generating the energy necessary for rotation, driven by ion translocation across a membrane (Terashima et al., 2008). The rotor part is comprised of the MS-ring, the C-ring, and a type III secretion system (T3SS)-like complex (Chevance and Hughes, 2008; Minamino et al., 2008). The MS-ring and the T3SS-like system are the first components of the flagellum to assemble, followed by other components (Li and Sourjik, 2011; Morimoto et al., 2014). The T3SS-like part interacts with its cytoplasmic partners FliH, FliI and FliJ to transport other flagellar components across the inner membrane (Minamino et al., 2011; Minamino and Imada, 2015). The assembly of both structures is stabilized through interactions with FliG from the C-ring (Li and Sourjik, 2011). The C-ring consists of the FliG, FliM and FliN proteins (Francis et al., 1994) (Fig. 1) and converts the energy from the stators' ion translocation into rotation (Minamino et al., 2008). This structure also performs a directionality switch, between clockwise (CW) or counter clockwise (CCW) directions, of the flagellar rotation (Carroll et al., 2020; Lee et al., 2010; Togashi et al.,
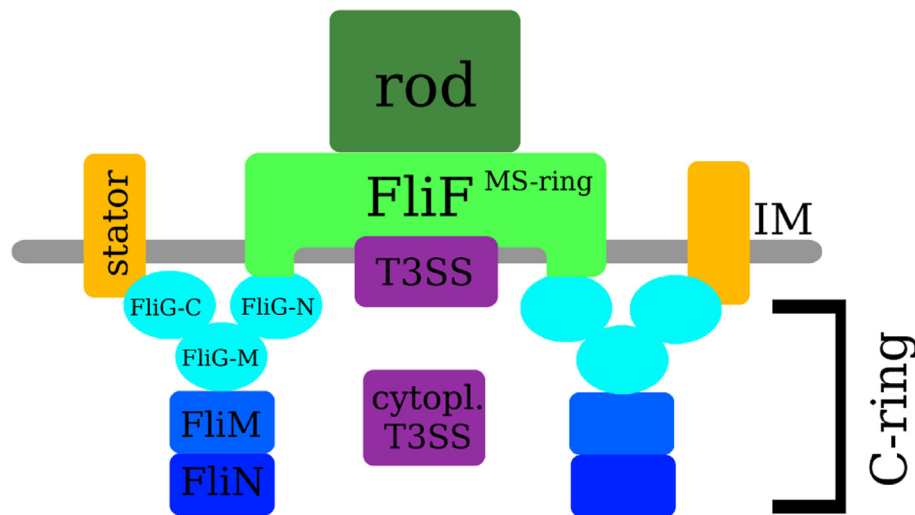
Fig. 1. Flagellar motor components. Overall structure of the flagellar motor. On the cytoplasmic side, the C-ring is composed of FliM, FliN and FliG that interacts with MS-ring, built of FliF proteins, residing in the periplasmic space and traversing the inner membrane (IM). The rotor (C-ring and MS-ring) interacts with stators traversing the inner membrane. FliG is central in joining the rotor rings and the stator. The T3SS-like system transports proteins through the inner membrane. FliG consists of N-terminal (FliG-N), middle (FliG-M) and C-terminal (FliG-C) domains. Rotor further transmits the movement upward in the flagellum, driving the rod.

1997). The changes in rotation direction induce a series of run and tumble motions, allowing bacteria to change directions and respond to environmental stimuli (Chaban et al., 2015).

FliG is one of the components of the C-ring and is central to the flagellar motor as it both transmits the torque from stator to rotor (Lloyd et al., 1996; Minamino et al., 2011) and co-folds with FliF of the MS-ring thereby supporting its assembly (Lynch et al., 2017; Terashima et al., 2020). FliG assembles into a 33-mer or 34-mer ring in *Salmonella* and *Vibrio alginolyticus*, although symmetry appears to be variable even within one species (Carroll et al., 2020; Thomas et al., 1999, 2006). The MS ring, which is composed of FliF, has been reported to have the stoichiometry of a 33-mer or 34-mer in *Salmonella* (Johnson et al., 2020; Kawamoto et al., 2021). Taking into account the co-folding of FliF and FliG (Lynch et al., 2017; Terashima et al., 2020) stable symmetry between the two rings can be expected. Small variations in assembly within species have been attributed to a lack of stabilization by the T3SS-like complex (Johnson et al., 2020) and construct truncation (Kawamoto et al., 2021) during heterologous expression in the case of FliF, and likewise could apply to FliG assembly. FliG consists of three distinct α-helical domains, including N-terminal (FliG-N), middle (FliG-M), and C-terminal (FliG-C) domains - the FliG-N domain binds FliF, the protein from which the MS-ring is constructed (Lee et al., 2010; Levenson et al., 2012). Each of the three individual domains as well as a full-length structure of FliG have been crystallized for various species (Brown et al., 2002; Lam et al., 2012; Lee et al., 2010; Lynch et al., 2017; Minamino et al., 2011; Xue et al., 2018). Several propositions about its conformation within a ring assembly have been made. Notably, they differ in the conformation of the region that connects the N-terminal domain to the middle domain – crystal structures have suggested that it can exist both as an extended long helix (Lee et al., 2010; Lynch et al., 2017) or two bent helices (Lynch et al., 2017; Xue et al., 2018). However, an experimentally determined structure of full-length FliG in the FliF-bound state is not available, and alternative monomeric models of the linker conformation based on cross-linking and coevolution data have also been proposed (Khan et al., 2018; Paul et al., 2011).

The overall composition of the flagellar motor, including the C-ring, has been observed in low resolution electron microscopy (EM) (Thomas et al., 2006) and cryo-electron tomography (cryo-ET) studies (Beeby et al., 2016), but no high resolution structure of an assembled C-ring has been resolved to date. There is no direct experimental evidence for the exact location of each domain of the C-ring proteins. Docking studies suggested that FliG-N may localize on the inside of the C-ring with the other two domains positioned relative to it in a "V-shape" (Carroll et al., 2020; Lee et al., 2010).

Given the mutual dependence between FliF and FliG (Lynch et al.,

2017; Terashima et al., 2020) and the central role of FliF in the assembly of the entire flagellum (Li and Sourjik, 2011; Morimoto et al., 2014), we now report a computational study exploring the conformation of FliG-N and its connection to FliG-M based on structural information from several species. Molecular dynamics (MD) simulations are a powerful tool for studying the conformational dynamics of proteins under the influence of different conditions, complementing data obtained from structural biology and integrative modelling (Hollingsworth and Dror, 2018). We use MD simulations here to study the dynamics of known FliG N-terminus crystal structures in different states of assembly, including in both physiologically relevant and crystallographic lattice unit cell environments, and conclude that the helices linking the N-terminus and middle domain cannot maintain the conformation observed in crystal structures while simulated in the physiologically-representative solution state. Based on our results, we propose an integrative model of FliG that connects the FliF-bound FliG N-terminal and middle domains with an extended helix, which we show is in agreement with cryo-ET (Carroll et al., 2020) and EM (Thomas et al., 2006) data for the C-ring. This model opens possibilities for an improved mechanistic understanding of energy transduction in bacterial flagella motors.

2. Methods

2.1. System setup

The H++ server (Gordon et al., 2005) was used to predict protonation state of ionizable residues, using $\varepsilon^{int} = 10$, $\varepsilon^{out} = 80$ at pH = 7.5, representing the physiological environment inside the bacterial cytoplasm (Kobayashi et al., 2000; Krulwich et al., 2011; Slonczewski et al., 2009). Two crystal structures of FliG PDB ID:5WUJ (Xue et al., 2018) and PDB ID:5TDY (Lynch et al., 2017) were simulated both in solution and under crystallographic unit cell conditions with pH of the crystal solution (Table S1). To assess reproducibility, we utilized both the CHARMM36m (Huang et al., 2016) and AMBER14SB (Maier et al., 2015) forcefields in separate simulations for each structure. For simulations in solution beginning from each structure, we used physiologically representative ion concentrations (150 mM NaCl), while the salinity in simulated crystallographic conditions was adjusted by removing sodium atoms that would be bound by sodium citrate in the crystallization solutions (Lynch et al., 2017; Xue et al., 2018). In addition, a variant of PDB ID 5WUJ with residues expressed and purified, but unresolved in electron density (residues 1 to 6 and 112 to 115 of FliG, and residues 518 to 523 and 559 to 567 of FliF respectively) were built with the ModLoop (Fiser and Sali, 2003) server. Additionally, the crystal structure of full length FliG (PDB ID:3HJL) (Lee et al., 2010) was simulated in solution using the CHARMM36m force field.

2.2. MD simulations

All MD simulations were performed with GROMACS 2018 package (Abraham et al., 2015). Equations of motion were integrated using leap-frog algorithm with 2 fs time step. We performed energy minimization using the steepest descents algorithm for 100,000 steps, followed by a 10 ns NPT equilibration with position restraints on the protein backbone atoms (using a force constant of 1000 kJ mol^{-1} nm^{-2}) for all structures. The unrestrained production runs in the NPT ensemble were run for 100–200 ns (Table S1). The TIP3P (Jorgensen et al., 1983) water model was used for all systems. Temperature for the solvated proteins at physiological conditions was maintained at 300 K using the v-rescale thermostat (Bussi et al., 2007), while a temperature mimicking the crystallization conditions was set to 289 K and 298 K for 5WUJ and 5TDY, respectively. The Parrinello-Rahman barostat (Parrinello and Rahman, 1981) was used for isotropic pressure coupling with reference pressure of 1 bar. Electrostatic interactions were calculated according to Particle Mesh Ewald (Darden et al., 1993) algorithm with a real space cut-off of 1.2 nm for CHARMM36m and 1.0 for AMBER14SB. For the calculation of van der Waals interactions, we applied a cut-off at 1.2 nm, switching the potential after 1.0 nm for CHARMM36m and 1.0 cut-off for AMBER14SB. The LINCS (Hess et al., 1997) algorithm was used for constraining bonds involving hydrogen atoms. Forcefield, simulation sampling, and relevant conditions for each system are summarized in Table S1. VMD (Humphrey et al., 1996) and PyMOL(D, 2002) were used for trajectory and structure visualization.

2.3. Model building

Sequences were aligned with MUSCLE software (Edgar, 2004; McWilliam et al., 2013). Homology models of full length *Helicobacter pylori* FliG were built in MODELLER (Webb and Sali, 2016). Initially a homology model of the N-terminus and the middle domain was built generating using the *H. pylori* structures (PDB-IDs: 5WUJ and 3USY) (Lam et al., 2013; Xue et al., 2018) and *Aquifex aeolicus* full-length structure (PDB-ID: 3HJL) (Lee et al., 2010). In addition, the linker region was defined as α-helical in MODELLER. From 2000 models, 10 with the best DOPE (Shen and Sali, 2006) and molpdf (Shen and Sali, 2006) scores were submitted to the SWISS-MODEL webserver (Schwede et al., 2003; Waterhouse et al., 2018) Structure Assessment and QMEAN (Benkert et al., 2008) evaluation tools. The model that was in both MODELLER score top 10 groups, had QMEAN score of 0.77 ± 0.06 and had no Ramachandran outliers was selected. To create the full-length model the crystal structure of the C-terminal and middle domains of *H. pylori* (PDB-ID: 3USY) (Lam et al., 2013) was overlaid the model over the middle domain that both structures share in VMD (Humphrey et al., 1996). Whole FliG rings were built by fitting three copies of the FliF-C/FliG and FliM-M complex in a segment of the *Vibrio alginolyticus* cryo-ET densities (Carroll et al., 2020), via manual placement and subsequent energy minimization. The system was then subjected to Molecular Dynamics Flexible Fitting (MDFF) (see below). For the *H.pylori* models, FliM-M was added by overlaying the model's middle domain with the crystal structure of the *H.pylori* middle domain and FliM middle domain (PDB-ID: 4FQ0 (Lam et al., 2013)) in Chimera (Pettersen et al., 2004). The middle copy of the three was used to build an entire ring from 34 copies of the monomer. The ring was placed in the cryo-ET density with the *Fit in Map* function in Chimera (Pettersen et al., 2004) using 20 Å resolution for the map created from the atomistic model, to obtain a final correlation.

2.4. Flexible fitting

MDFF is used to dynamically fit atomic coordinates into experimental density maps (Trabuco et al., 2009). An additional external potential derived from an experimental map is defined on a grid to drive gradual fitting of coordinates. All MDFF simulations were performed on a trimeric unit of the *H.pylori* FliF-C/FliG/FliM-M complex for the CW or CCW cryo-ET density maps from *V.alginolyticus* (Carroll et al., 2020). All such simulations were run using NAMD2.9 (Trabuco et al., 2009) with the CHARMM36 FF (Huang and Mackerell, 2013) without solvent. The nonbonded interactions were switched off between 1.0 and 1.2 nm using a force-switching method (Steinbach and Brooks, 1994). Langevin dynamics was used to maintain the temperature at 300 K with a coupling coefficient of 5 ps^{-1}. For electrostatic interactions, a dielectric constant of 80 was used. The flexible fitting was run in 10–15 separate simulation steps, with increased scaling factors from 0.1 to 15. The bias was applied to all non-hydrogen atoms with atom-dependent mass weighting. Additional restraints in MDFF were used to maintain correct chiral centres, peptide bond conformations, and secondary structures of each protein. All simulation systems were generated using CHARMM-GUI through Map Utilizer (Qi et al., 2017).

2.5. Analysis

The fitting between simulation coordinates and experimental density map was calculated in Chimera (Pettersen et al., 2004). Fit in Map tool locally maximizes the overlap between atomic coordinates and the density map. The correlation coefficient was calculated as minimum mean cosine angle between the vectors derived from experimental and simulation map calculated on the grid. It can vary from −1 to 1, from not correlated to identical respectively.

3. Results and discussion

3.1. Solution dynamics of FliG-N reveal conformational instability of helices 6 and 7

To probe the conformational dynamics of FliG, we first focused on the crystal structure from *H. pylori*. In this structure (PDB ID: 5WUJ) (Xue et al., 2018), FliG-N is bound to the C-terminal fragment of FliF (FliF-C); the two fragments are entirely α-helical, consisting of 7 FliG helices and two FliF helices within the complex, and with 6 such complexes in the unit cell (Fig. 2). FliG helices 6 and 7 are in a bent conformation due to hydrophobic interactions between them and helices 3 and 4 of another complex of the crystal lattice (Fig. S1).

We first used the H++ webserver (Gordon et al., 2005) to calculate the pK$_a$ for all titratable residues. The results indicated that residue E91 (surrounded by a negatively charged environment) may be either protonated or deprotonated (Fig. S2). Simulations of a single FliG-N in the absence of the FliF-C showed that across multiple replicas, isolated FliG-N was highly unstable and spontaneously acquired very different conformations in each run, consistent with backbone RMSDs over entire protein (Fig. S3). While helices 6 and 7 deviated from initial position the most, the remainder of the domain conformation also collapsed due to loss of interactions with FliF (Fig. S3). There was no correlation between the observed conformational changes and the protonation state of E91. The only other crystal structure of the N-terminal domain is found in the full-length FliG structure from *A. aeolicus* in the absence of FliF (PDB ID: 3HJL) (Lee et al., 2010). None of the conformations FliG-N adopted during simulation were similar to this; helices 1 to 5 did not pack in a comparable way, whilst helices 6 and 7 did not adopt the extended conformation observed in the *A. aeolicus* structure. These results are in agreement with experimental data, which show that FliG and FliF co-fold and require each other to assemble (Lynch et al., 2017; Terashima et al., 2020). Thus, we did not pursue this state further.

We next focused on the complex formed between *H. pylori* FliG-N and FliF-C. Examination of the stability of individual helices during triplicate simulations revealed that FliG helices 2 to 5 form a stable core of the complex (Fig. S4) while FliG helices 6 and 7 have the highest RMSD (Fig. 3). The simulations did not converge, with divergent conformations adopted for helices 6 and 7 across replicas. In addition, to characterize the movement of helices 6 and 7, angles between the helices were
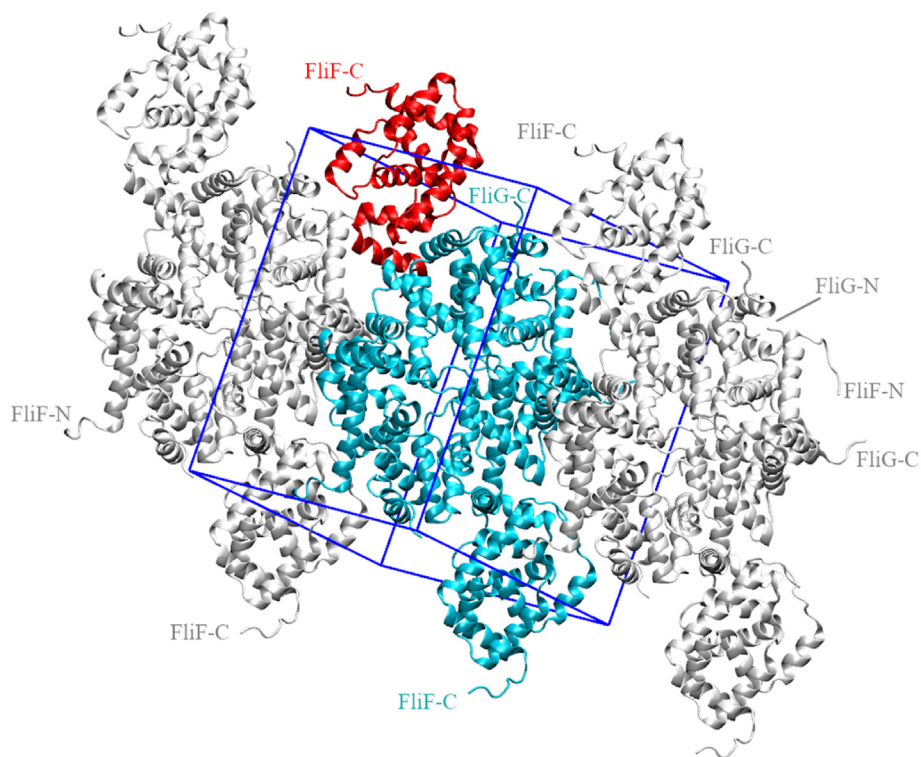
Fig. 2. Unit cell of crystal structure 5WUJ. Unit cell box is shown with 6 FliG-N/FliF-C complexes, one of which is colored in red; molecules in neighbouring unit cells are shown in grey. Single complex is shown in S2. (For interpretation of the references to color in this figure legend, the reader is referred to the Web version of this article.)
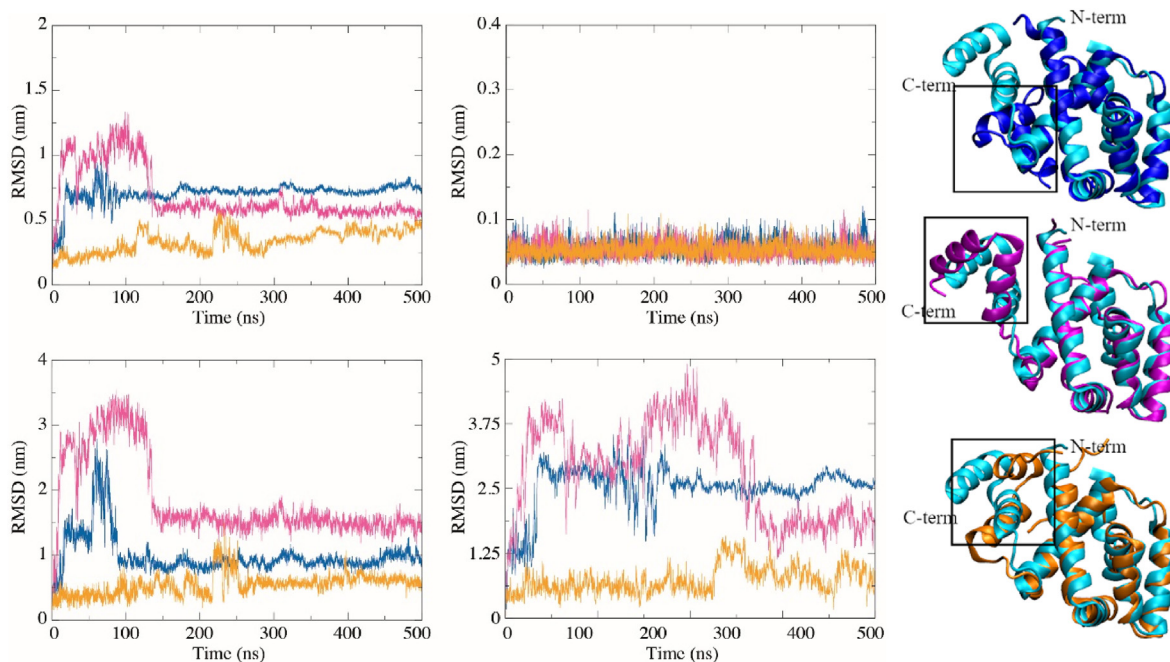

Fig. 3. Structural drift of 5WUJ complex in solution. Backbone RMSD after fitting against backbone of protein core for: whole protein (top left), FliG helix 2 (top right), FliG helix 6 (bottom left), and FliG helix 7 (bottom right). Different colors represent three independent runs. On the right, snapshots are shown for the three runs (blue, magenta, orange) after 500 ns versus the initial structure (cyan). Box indicates position of helices 6 and 7. (For interpretation of the references to color in this figure legend, the reader is referred to the Web version of this article.)

measured. The angle was defined for axes between the Cα atoms of the first and last residue of each helix. The angle between helices 6 and 7 in the crystal structure is $-49°$ while in the three simulation runs it was on average $-54 \pm 10°$, $-51 \pm 14°$ and $-50 \pm 19°$; the larger standard deviations are reflective of high mobility. In comparison, the same measurement was made for the angle between helices 3 and 4 that are part of the stable FliG core, yielding $-44°$ in the crystal structure and $-42 \pm 5°$, $-41 \pm 6°$ and $-42 \pm 5°$ in the simulations.

3.2. Crystal contacts stabilize helix 6 and 7 of FliG-N

Crystallographic resolution and artefacts can have a crucial impact on the interpretation of structural data from which molecular properties of biological macromolecules are derived. The crystallographic environment can alter the binding properties of a ligand (Søndergaard et al., 2009) and can also introduce bias in the conformation of sidechains (Arpino et al., 2012) or influence the presence/absence of other structural elements, such as ions (Krah and Takada, 2016). Moreover, discerning local environmental details, such as the distinction between water molecules and ions (Krah et al., 2020), as well as more substantial structural issues such as distinguishing between crystal packing versus genuine oligomerization interfaces, are often not straightforward (Carugo and Argos, 1997; Dey et al., 2018; Luo et al., 2015; Sardis and Economou, 2010).

The interactions between FliG-N/FliF-C complexes observed in the 5WUJ structure's crystal lattice have been proposed to be of biological relevance for FliG assembly in a ring (Xue et al., 2018). Motivated by the unstable conformations of helices 6 and 7 of the monomer in solution, we carried out simulations of a tetramer of FliG-N/FliF-C complexes in solution (FliG-N/FliF-C^{tetr}), which corresponded to the crystallographic asymmetric unit assembly (Fig. S5), in order to probe if crystal lattice interactions may play a role in artefactually determining the positions and bent conformation of helices 6 and 7 in FliF-N. Our simulations indeed revealed that the flanking FliG-N monomers on the periphery of the complex were unstable (helices 6 and 7 on one side, and helices 1 to 5 on other), while those surrounded by other proteins in the center of the tetrameric complex were more stable (Fig. S5). There was no noticeable dependence of this behavior upon forcefield or E91 protonation state (Figs. S6–S9).

Simulations containing the same FliG-N/FliF-C complexes were subsequently set up, but with periodic boundary conditions imposed such that the crystallographic unit cell conditions encompassing all crystal contacts were replicated (FliG-N/FliF-C^{cryst}), thereby enabling us to further probe the effects of crystal packing upon FliG helices 6 and 7. Simulation of FliG-N/FliF-C^{cryst} revealed that these elements are indeed stabilized by crystal contacts, as evidenced by a reduction in final plateaued RMSD for the entire backbone of each FliG-N from ~0.2 to 0.3 nm (Fig. 4), irrespective of forcefield or E91 protonation state

(Figs. S10–S16). Consistent with this, the average angles measured between helices 6 and 7 in FliG-N/FliF-C^{cryst} for the 6 copies in the unit cell were −53 ± 3°, −48 ± 4°, −57 ± 7, −49 ± 3°,-54 ± 4°,-54 ± 6°. Thus, significantly less variation was observed in this angle in FliG-N/FliF-C^{cryst} compared to the fully solvated FliG-N/FliF-C system. On the other hand, a comparable stability was observed for the core helices 3 and 4, with average angles for the 6 copies in FliG-N/FliF-C^{cryst} of 46 ± 4°, −46 ± 5°, −47 ± 4°, −40 ± 4°, −45 ± 4°, and −48 ± 4°.

To test whether the stabilization of helices 6 and 7 in the bent conformation observed for FliG-N/FliF-C^{cryst} is structure or species specific, we also performed the same set of simulations described above for the corresponding structure of the FliG-N/FliF-C complex from *Thermotoga maritima* (PDB ID: 5TDY (Lynch et al., 2017)). The *T. maritima* structure has two conformations (Fig. S17) – the first is composed of 6 FliG helices lacking the small N-terminal helix found in *H. pylori* and two FliF helices – overall with a highly similar fold to that observed in PDBID:5WUJ (Xue et al., 2018) (RMSD = 2.4 Å over 427 backbone atoms across FliG-N/FliF-C (Fig. S18)) and the sequence share 36.3% similarity. In the second conformation, helix 5 is merged in an extended helix together with helix 6, which is different from the extended conformation of *Aquifex aeolicus*. During comparative simulations, both conformations of FliG-N bound to FliF-C were destabilized in the region spanning helices 6 and 7 in solution for the first conformation and the extended helix for the second conformation, and were stabilized under unit cell conditions (Figures S19-S22, S24-S25), similarly to the results obtained for the *H. pylori* structure. Our observations and the conserved sequence and length of FliG confirms that the conformational dynamics of the isolated FliG-FliF protein complex are likely species independent. We also assessed the dynamics of the N-terminal region in the context of the *Aquifex aeolicus* full length structure, and while the extended helix seems to be destabilized during simulation there was also a substantial structural drift across the entire molecule (Fig. S23). The N-terminal region itself maintained its conformation indicating that the presence of other domains is also a stabilizing factor (Fig. S23). In addition, while the sequence is conserved, there are local sequence differences in the N-terminal region, with more negatively charged residues in the associated domain (Fig. S27), and it is therefore likely that more extensive conformational sampling would be required to observe its destabilization in the case of *Aquifex aeolicus* as opposed to *Helicobacter pylori*.
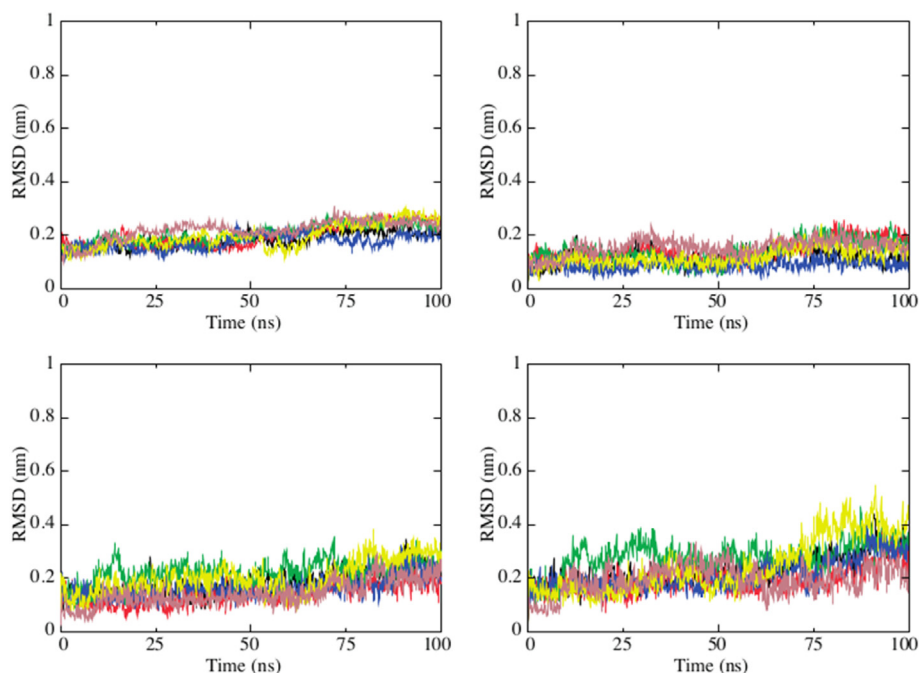

Fig. 4. Structural drift of FliG-N/FliF-C^{cryst} in the unit cell. Backbone RMSD after fitting against backbone of protein against whole protein (top left) and backbone of protein core for: FliG helix2 (top right), FliG helix6 (bottom left), and FliG helix 7 (bottom right). System used the CHARMM36m force field with E91 deprotonated; different colors represent each FliG-FliF complex in the unit cell. (For interpretation of the references to color in this figure legend, the reader is referred to the Web version of this article.)

We have thus demonstrated that a specific conformation of helices 6 and 7 of the FliG N-terminal domain is enforced by crystal contacts in structures from two different species. The instability of FliG helices 6 and 7 in a bent conformation in solution opens a discussion about the likely biological conformation of this part of FliG in the whole flagellar complex. It should also be noted that the bent conformation has been shown not to match the solution SAXS envelope of *T. maritima* monomer (Lynch et al., 2017). The exact conformation relevant to the ring assembly, however, has remained elusive.

3.3. Modelling of full-length FliG in a ring assembly

Motivated by our simulation results, which indicate that available crystal structures of the FliG/FliF complex do not reflect the biologically relevant conformation of FliG in the ring assembly, we investigated an alternative, extended conformation of helices 6 and 7. An integrative model composed of the *H. pylori* FliG N-terminal and middle domains was built using structural data for separately crystallized respective domains (PDB ID:5WUJ (Xue et al., 2018) and 3USW (Lam et al., 2012)) and a full length apo-FliG structure from *A. aeolicus* (PDB ID:3HJL (Lee et al., 2010)). The latter features an extended helix between the N-terminus and middle domain instead of two separate helices. The model was further extended to a full length *H. pylori* FliG model by incorporating information from the *H. pylori* middle and C-terminal domains as resolved crystallographically (PDB ID:3USY) (Lam et al., 2012) (Fig. 5). Thus, the model included crystallographic information for all three FliG domains and the two FliF helices bound to FliG.

Unlike for *A. aeolicus*, for *H. pylori* two different conformations of the C-terminal domain have been observed crystallographically, and were proposed to represent states relevant to clock-wise (CW) and counter-clockwise (CCW) conformations (Lam et al., 2012), but which corresponds to which state is unknown. Therefore, a second model replacing one conformation (PDB-ID: 3USY (Lam et al., 2012)) of the C-terminal

domain with another crystallized conformation (PDB-ID: 3USW (Lam et al., 2012)) was built, while preserving the linker from the first structure as it was not resolved in the other (Fig. 5). The linker between middle and C-terminal domains is not structured in either *H. pylori* crystal structures, indicating that in *H. pylori* the linker between the two domains is flexible or that it may adopt different conformations under certain conditions.

Both models were docked into the cryo-ET maps of the *V. alginolyticus* rotor (EMD-21819 and EMD-21837) (Carroll et al., 2020) in the presumed locations of the N-terminal, middle, and C-terminal domains (Fig. 6), in accordance with previous docking studies of the highly comparable EM map of the *Salmonella* C-ring (Lee et al., 2010; Thomas et al., 2006). A more recent cryo-ET study of a *Vibrio* motor shows joining density between the likely locations of the N-terminus and middle domain in the C-ring (Carroll et al., 2020). This, and the reasonable sequence identity between *H. pylori* and *V. alginolyticus* FliG (27.6%), supports our proposed model. Unlike the previously proposed ring assembly of *H. pylori* FliG-N/FliF-C only that includes FliG helices 6 and 7 in a bent conformation (Xue et al., 2018), our full-length FliG model accounts for joining of all FliG domains while fitting in the cryo-ET density.

We added FliM to our FliF-C/FliG model and manually placed the trimer into a segment of CW or CCW density from *V. alginolyticus* (Carroll et al., 2020) corresponding to the presumed location of FliF-C, FliG and FliM-M. We next took a MDFF simulation approach to create a better fit of the structure with the experimental density. The middle copy after applying MDFF was used to create 34-mer FliG/FliM rings with two C-terminal conformations within both densities. While all rings after fitting into the cryo-ET density had a correlation of over 0.94, other crucial structural features were evaluated to select the most reasonable models (Fig. 6). We chose a ring model corresponding to CCW density with a 0.99 correlation when using the simulated map at 20 Å resolution, and a CW model with 0.95 correlation. Both models were built in which the starting model adopted the C-terminal conformation as resolved in
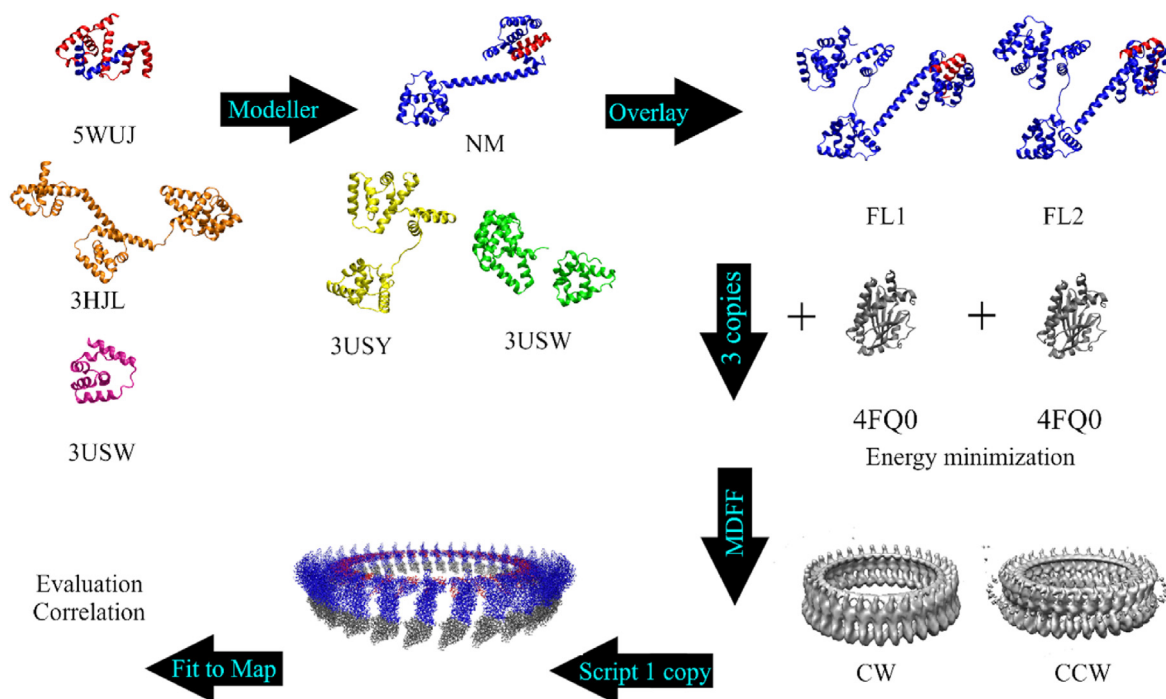

Fig. 5. Model building workflow for full-length FliG ring. Homology model of FliG-NM was built based on three crystal structures, and subsequently used to construct two full-length FliG models (FL1 and FL2). FliG rings were built from these two models, using two cryo-ET density maps corresponding to clockwise (CW) and counter-clockwise (CCW) C-rings and two possible positions (C-terminal domain interacting with middle domain of the same ("0" position) or neighbouring ("-1 position") FliG molecule). After building rings in all possible combinations, best models were picked by visual evaluation and subjected to energy minimization in GROMACS.
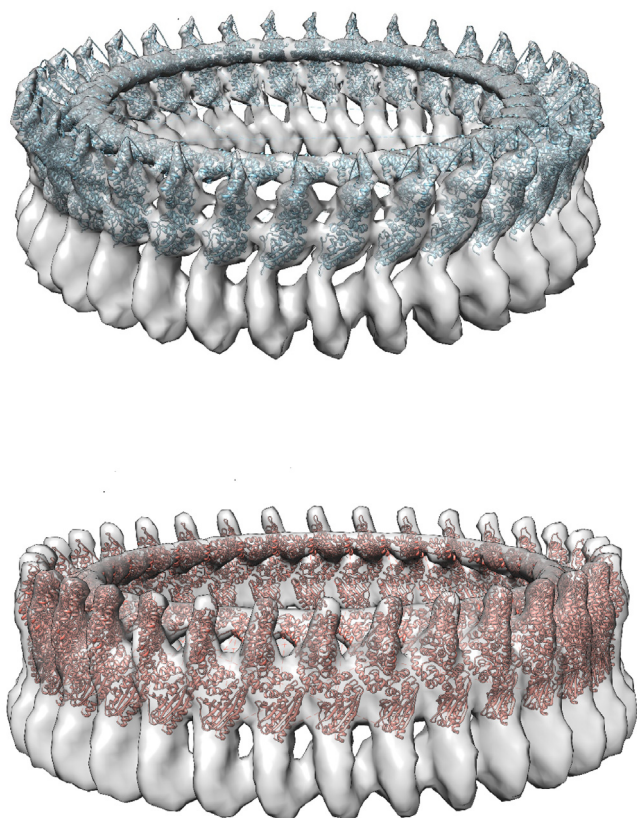
Fig. 6. Full length *H. pylori* FliF-C/FliG/FliM-M 34-mer model docking into CCW and CW rotor cryo-ET density of *V. alginolyticus*. Top – full length FliG/FliM-M model in CCW density, bottom – full length FliG model in CW density. The density is oriented with the FliN layer at the bottom of the image, and the FliF/membrane layer at the top.

PDB ID:3USY (Fig. S26). This does not exclude that other crystallized conformations are relevant in other functional conditions, for example, during the assembly process. The cryo-ET study of *V. alginolyticus* predicted that in the transition from the CW to CCW states of the rotor, the C-terminal domain may shift from interacting with the middle domain of the same monomer ("0" position) to interacting with the middle domain of a neighbouring, previous monomer ("-1" position) (Carroll et al., 2020) (Fig. 5). In another study, this switch was proposed to drive assembly of the FliG ring instead (Baker et al., 2016). The proposed position of the FliG C-terminal domain in both of our ring models is CW^0. There is no consensus on how the FliG C-terminal domain would be placed in CW or CCW states, and our ring model represents only one of the possibilities. While MDFF changes the overall shape of the model and linkers during fitting to the density, our CCW model retains individual domains that are similar to their starting position. The C-terminal region is closer to middle domain, unlike in crystal structure. The helix linking the N-terminal and middle domains is not straight like in the starting model, but does not form a bent conformation as observed crystallographically, but instead assumes a somewhat intermediate position. In our CW model the helix remains straight, but the two helices at the C-terminus interact with this extended helix closer to FliG-M. The N-terminus to middle domain linker transition from fully straight to partially bent may have functional significance in transitioning between CCW and CW states (Fig. S26). A previous crosslinking experiment using *T. maritima* (Paul et al., 2011) contradicts the assumption that the N-terminal and middle domains are located in the locations predicted in our work and the *Vibrio* cryo-ET studies (Carroll et al., 2020). However, the protein in the Paul et al. (2011) experiment (Paul et al., 2011) was

produced by heterologous overexpression in *E. coli* without presence of FliF in a 1:1 ratio, which has been shown to be crucial for folding of the N-terminal domain (Lynch et al., 2017; Terashima et al., 2020), suggesting it may not represent conformation relevant to the ring, but may instead be found in another, transport relevant state; we indeed observed the FliG N-terminal domain adopting various conformations in the absence of FliF (Fig. S3). While mutation of the crystal contact interface between FliG helices 3–4 and helices 6–7 in their bent conformation has been shown to affect motility in *E.coli* (Xue et al., 2018), this may compromise the macro phenotype through interference with FliG function in other ways.

Due to the flexibility of the connection between middle and C-terminal domains in *H. pylori* crystal structures (Xue et al., 2018), the C-terminal domain could localize at different positions within the density, but our docking demonstrates that an extended helix between the middle and N-terminal domains is compatible with the cryo-ET data. While the bent conformation of the linker between the N-terminal and middle domains may have functional relevance during the assembly or transportation, within the ring it cannot conceivably join the two domains according to the *Vibrio* cryo-ET maps. The length of FliG is also mostly conserved (Fig. S27), but the diameter of the C-ring is known to vary among species (Beeby et al., 2016), the most prominent example being *B. burgdorferi* C-ring ring that has 46-fold symmetry (Chang et al., 2020). The *H.pylori* ring is possibly wider according to a low resolution cryo-ET study using the entire motor (Qin et al., 2017). We have modelled a 34-mer to match the density based on the highest-resolution map available, though it is possible that the number of subunits within the ring is variable among species to account for diameter differences.

4. Conclusions

In conclusion, combining our data show that the region joining FliG N-terminus and middle domain likely forms an extended helix in a functional ring assembly. In addition, our simulations provide support of how FliF is needed for the structural stability of FliG in *Helicobacter pylori*, in agreement with previous interpretations of experimental data (Levenson et al., 2012). Further work needs to be done on studying FliG domain interactions, possible differences between C-terminus conformations and changes depending on e.g. CW or CCW rotational direction or e.g. to accommodate binding of T3SS, in order to build a comprehensive model of the C-ring as well as study possible stoichiometry differences in different species.

CRediT authorship contribution statement

Dagnija Tupiņa: Methodology, Software, Formal analysis, Visualization, Investigation, Writing – original draft, Writing – review & editing. **Alexander Krah:** Methodology, Formal analysis, Visualization, Investigation, Writing – original draft, Writing – review & editing. **Jan K. Marzinek:** Methodology, Formal analysis, Visualization, Investigation, Writing – review & editing. **Lorena Zuzic:** Methodology, Software. **Adam A. Moverley:** Methodology, Software. **Chrystala Constantinidou:** Conceptualization, Supervision, Writing – review & editing. **Peter J. Bond:** Conceptualization, Supervision, Writing – original draft, Writing – review & editing.

Declaration of competing interest

The authors declare that they have no known competing financial interests or personal relationships that could have appeared to influence the work reported in this paper.

Appendix A. Supplementary data

Supplementary data to this article can be found online at https://doi.org/10.1016/j.crstbi.2022.02.002.

References

Abraham, M.J., Murtola, T., Schulz, R., Páll, S., Smith, J.C., Hess, B., Lindah, E., 2015. Gromacs: high performance molecular simulations through multi-level parallelism from laptops to supercomputers. SoftwareX 1–2, 19–25. https://doi.org/10.1016/j.softx.2015.06.001.

Arpino, J.A.J., Rizkallah, P.J., Jones, D.D., 2012. Crystal structure of enhanced green fluorescent protein to 1.35 Å resolution reveals alternative conformations for Glu222. PLoS One 7, e47132. https://doi.org/10.1371/journal.pone.0047132.

D, W.L., 2002. The PyMOL Molecular Graphics System.

Baker, M.A.B., Hynson, R.M.G., Ganuelas, L.A., Mohammadi, N.S., Liew, C.W., Rey, A.A., Duff, A.P., Whitten, A.E., Jeffries, C.M., Delalez, N.J., Morimoto, Y.V., Stock, D., Armitage, J.P., Turberfield, A.J., Namba, K., Berry, R.M., Lee, L.K., 2016. Domain-swap polymerization drives the self-assembly of the bacterial flagellar motor. Nat. Struct. Mol. Biol. 23, 197–203. https://doi.org/10.1038/nsmb.3172.

Beeby, M., Ribardo, D.A., Brennan, C.A., Ruby, E.G., Jensen, G.J., Hendrixson, D.R., 2016. Diverse high-torque bacterial flagellar motors assemble wider stator rings using a conserved protein scaffold. Proc. Natl. Acad. Sci. U. S. A. 113, E1917–E1926. https://doi.org/10.1073/pnas.1518952113.

Benkert, P., Tosatto, S.C.E., Schomburg, D., 2008. QMEAN: a comprehensive scoring function for model quality assessment. Proteins Struct. Funct. Genet. 71, 261–277. https://doi.org/10.1002/prot.21715.

Brown, P.N., Hill, C.P., Blair, D.F., 2002. Crystal structure of the middle and C-terminal domains of the flagellar rotor protein FliG. EMBO J. 21, 3225–3234. https://doi.org/10.1093/emboj/cdf332.

Bussi, G., Donadio, D., Parrinello, M., 2007. Canonical sampling through velocity rescaling. J. Chem. Phys. 126, 014101. https://doi.org/10.1063/1.2408420.

Carroll, B.L., Nishikino, T., Guo, W., Zhu, S., Kojima, S., Homma, M., Liu, J., 2020. The flagellar motor of Vibrio alginolyticus undergoes major structural remodeling during rotational switching. Elife 9, e61446. https://doi.org/10.7554/eLife.61446.

Carugo, O., Argos, P., 1997. Protein-protein crystal-packing contacts. Protein Sci. 6, 2261–2263.

Chaban, B., Hughes, H.V., Beeby, M., 2015. The flagellum in bacterial pathogens: for motility and a whole lot more. Semin. Cell Dev. Biol. 46, 91–103. https://doi.org/10.1016/j.semcdb.2015.10.032.

Chang, Y., Zhang, K., Carroll, B.L., Zhao, X., Charon, N.W., Norris, S.J., Motaleb, M.A., Li, C., Liu, J., 2020. Molecular mechanism for rotational switching of the bacterial flagellar motor. Nat. Struct. Mol. Biol. https://doi.org/10.1038/s41594-020-0497-2.

Chevance, F.F.V., Hughes, K.T., 2008. Coordinating assembly of a bacterial macromolecular machine. Nat. Rev. Microbiol. 6, 455–465. https://doi.org/10.1038/nrmicro1887.

Darden, T., York, D., Pedersen, L., 1993. Particle mesh Ewald: an N·log(N) method for Ewald sums in large systems. J. Chem. Phys. 98, 10089–10092. https://doi.org/10.1063/1.464397.

Dey, S., Ritchie, D.W., Levy, E.D., 2018. PDB-wide identification of biological assemblies from conserved quaternary structure geometry. Nat. Methods 15, 67–72. https://doi.org/10.1038/nmeth.4510.

Edgar, R.C., 2004. MUSCLE: multiple sequence alignment with high accuracy and high throughput. Nucleic Acids Res. 32, 1792–1797. https://doi.org/10.1093/nar/gkh340.

Fiser, A., Sali, A., 2003. ModLoop: automated modeling of loops in protein structures. Bioinformatics 19, 2500–2501. https://doi.org/10.1093/bioinformatics/btg362.

Francis, N.R., Sosinsky, G.E., Thomas, D., DeRosier, D.J., 1994. Isolation, characterization and structure of bacterial flagllar motors containing the switch complex. J. Mol. Biol. 235, 1261–1270.

Gordon, J.C., Myers, J.B., Folta, T., Shoja, V., Heath, L.S., Onufriev, A., 2005. H++: a server for estimating pKas and adding missing hydrogens to macromolecules. Nucleic Acids Res. 33, W368–W371. https://doi.org/10.1093/nar/gki464.

Hess, B., Bekker, H., Berendsen, H.J.C., Fraaije, J.G.E.M., 1997. LINCS: a linear constraint solver for molecular simulations. J. Comput. Chem. 18, 1463–1472. https://doi.org/10.1002/(SICI)1096-987X(199709)18:12<1463::AID-JCC4>3.0.CO;2-H.

Hollingsworth, S.A., Dror, R.O., 2018. Molecular dynamics simulation for all. Neuron 99, 1129–1143. https://doi.org/10.1016/j.neuron.2018.08.011. Molecular.

Huang, J., Mackerell, A.D., 2013. CHARMM36 all-atom additive protein force field: validation based on comparison to NMR data. J. Comput. Chem. 34, 2135–2145. https://doi.org/10.1002/jcc.23354.

Huang, J., Rauscher, S., Nawrocki, G., Ran, T., Feig, M., De Groot, B.L., Grubmüller, H., MacKerell, A.D., 2016. CHARMM36m: an improved force field for folded and

intrinsically disordered proteins. Nat. Methods 14, 71–73. https://doi.org/10.1038/nmeth.4067.

Humphrey, W., Dalke, A., Schulten, K., 1996. Visual molecular dynamics. J. Mol. Graph. 14, 38–34.

Johnson, S., Fong, Y.H., Deme, J.C., Furlong, E.J., Kuhlen, L., Lea, S.M., 2020. Symmetry mismatch in the MS-ring of the bacterial flagellar rotor explains the structural coordination of secretion and rotation. Nat. Microbiol. 5, 966–975. https://doi.org/10.1038/s41564-020-0703-3.

Jorgensen, W.L., Chandrasekhar, J., Madura, J.D., Impey, R.W., Klein, M.L., 1983. Comparison of simple potential functions for simulating liquid water. J. Chem. Phys. 79, 926–935. https://doi.org/10.1063/1.445869.

Kawamoto, A., Miyata, T., Makino, F., Kinoshita, M., Imada, K., Kato, T., Namba, K., 2021. Native structure of flagellar MS ring is formed by 34 subunits with 23-fold and 11-fold subsymmetries. Nat. Commun. 12, 4223. https://doi.org/10.1038/s41467-021-24507-9.

Khan, S., Guo, T.W., Misra, S., 2018. A coevolution-guided model for the rotor of the bacterial flagellar motor. Sci. Rep. 8, 11754. https://doi.org/10.1038/s41598-018-30293-0.

Kobayashi, H., Saito, H., Kakegawa, T., 2000. Bacterial strategies to inhabit acidic environments. J. Gen. Appl. Microbiol. 46, 235–243.

Krah, A., Takada, S., 2016. On the ATP binding site of the ε subunit from bacterial F-type ATP synthases. Biochim. Biophys. Acta Bioenerg. 1857, 332–340. https://doi.org/10.1016/j.bbabio.2016.01.007.

Krah, A., Huber, R.G., Zachariae, U., Bond, P.J., 2020. On the ion coupling mechanism of the MATE transporter ClbM. Biochim. Biophys. Acta Biomembr. 1862, 183137. https://doi.org/10.1016/j.bbamem.2019.183137.

Krulwich, T.A., Sachs, G., Padan, E., 2011. Molecular aspects of bacterial pH sensing and homeostasis. Nat. Rev. Microbiol. 9, 330–343. https://doi.org/10.1038/nrmicro2549.

Lam, K.-H., Ling, T.K.-W., Chan, S.-O., Au, S.W.-N., Lam, Y.-W., Ip, W.-S., 2012. Multiple conformations of the FliG C-terminal domain provide insight into flagellar motor switching. Structure 20, 315–325. https://doi.org/10.1016/j.str.2011.11.020.

Lam, K.H., Lam, W.W.L., Wong, J.Y.K., Chan, L.C., Kotaka, M., Ling, T.K.W., Jin, D.Y., Ottemann, K.M., Au, S.W.N., 2013. Structural basis of FliG-FliM interaction in Helicobacter pylori. Mol. Microbiol. 88, 798–812. https://doi.org/10.1111/mmi.12222.

Lee, L.K., Ginsburg, M.A., Crovace, C., Donohoe, M., Stock, D., 2010. Structure of the torque ring of the flagellar motor and the molecular basis for rotational switching. Nature 466, 996–1000. https://doi.org/10.1038/nature09300.

Levenson, R., Zhou, H., Dahlquist, F.W., 2012. Structural insights into the interaction between the bacterial flagellar motor proteins FliF and FliG. Biochemistry 51, 5052–5060. https://doi.org/10.1021/bi3004582.

Li, H., Sourjik, V., 2011. Assembly and stability of flagellar motor in Escherichia coli. Mol. Microbiol. 80, 886–899. https://doi.org/10.1111/j.1365-2958.2011.07557.x.

Lloyd, S.A., Tang, H., Wang, X., Billings, S., Blair, D.F., 1996. Torque generation in the flagellar motor of Escherichia coli: evidence of a direct role for FliG but not for FliM or FliN. J. Bacteriol. 178, 223–231. https://doi.org/10.1128/jb.178.1.223-231.1996.

Luo, J., Liu, Z., Guo, Y., Li, M., 2015. A structural dissection of large protein-protein crystal packing contacts. Sci. Rep. 5, 14214. https://doi.org/10.1038/srep14214.

Lynch, M.J., Levenson, R., Kim, E.A., Sircar, R., Blair, D.F., Dahlquist, F.W., Crane, B.R., 2017. Co-folding of a FliF-FliG split domain forms the basis of the MS:C ring interface within the bacterial flagellar motor. Structure 25, 317–328. https://doi.org/10.1016/j.str.2016.12.006.

Maier, J.A., Martinez, C., Kasavajhala, K., Wickstrom, L., Hauser, K.E., Simmerling, C., 2015. ff14SB: improving the accuracy of protein side chain and backbone parameters from ff99SB. J. Chem. Theor. Comput. 11, 3696–3713. https://doi.org/10.1021/acs.jctc.5b00255.

McWilliam, H., Li, W., Uludag, M., Squizzato, S., Park, Y.M., Buso, N., Cowley, A.P., Lopez, R., 2013. Analysis tool web services from the EMBL-EBI. Nucleic Acids Res. 41, W597–W600. https://doi.org/10.1093/nar/gkt376.

Minamino, T., Imada, K., 2015. The bacterial flagellar motor and its structural diversity. Trends Microbiol. 23, 267–274. https://doi.org/10.1016/j.tim.2014.12.011.

Minamino, T., Imada, K., Namba, K., 2008. Molecular motors of the bacterial flagella. Curr. Opin. Struct. Biol. 18, 693–701. https://doi.org/10.1016/j.sbi.2008.09.006.

Minamino, T., Morimoto, Y.V., Hara, N., Namba, K., 2011. An energy transduction mechanism used in bacterial flagellar type III protein export. Nat. Commun. 2. https://doi.org/10.1038/ncomms1488.

Minamino, T., Nakamura, S., Imada, K., Namba, K., Morimoto, Y.V., Kinoshita, M., 2011. Structural insight into the rotational switching mechanism of the bacterial flagellar motor. PLoS Biol. 9, e1000616. https://doi.org/10.1371/journal.pbio.1000616.

Morimoto, Y.V., Kami-ike, N., Minamino, T., Che, Y.-S., Hiraoka, K.D., Ito, M., Bai, F., Namba, K., 2014. Assembly and stoichiometry of FliF and FlhA in Salmonella flagellar basal body. Mol. Microbiol. 91, 1214–1226. https://doi.org/10.1111/mmi.12529.

Parrinello, M., Rahman, A., 1981. Polymorphic transitions in single crystals: a new molecular dynamics method. J. Appl. Phys. 52, 7182–7190. https://doi.org/10.1063/1.328693.

Paul, K., Gonzalez-Bonet, G., Bilwes, A.M., Crane, B.R., Blair, D., 2011. Architecture of the flagellar rotor. EMBO J. 30, 2962–2971. https://doi.org/10.1038/emboj.2011.188.

Pettersen, E.F., Goddard, T.D., Huang, C.C., Couch, G.S., Greenblatt, D.M., Meng, E.C., Ferrin, T.E., 2004. UCSF Chimera - a visualization system for exploratory research and analysis. J. Comput. Chem. 25, 1605–1612. https://doi.org/10.1002/jcc.20084.

Qi, Y., Lee, J., Singharoy, A., McGreevy, R., Schulten, K., Im, W., 2017. CHARMM-GUI MDFF/xMDFF utilizer for molecular dynamics flexible fitting simulations in various environments. J. Phys. Chem. B 121, 3718–3723. https://doi.org/10.1021/acs.jpcb.6b10568.

Qin, Z., Lin, W. ting, Zhu, S., Franco, A.T., Liu, J., 2017. Imaging the motility and chemotaxis machineries in Helicobacter pylori by cryo-electron tomography. J. Bacteriol. 199, e00695-16. https://doi.org/10.1128/JB.00695-16.

Sardis, M.F., Economou, A., 2010. SecA: a tale of two protomers: MicroReview. Mol. Microbiol. 76, 1070–1081. https://doi.org/10.1111/j.1365-2958.2010.07176.x.

Schwede, T., Kopp, J., Guex, N., Peitsch, M.C., 2003. SWISS-MODEL: an automated protein homology-modeling server. Nucleic Acids Res. 31, 3381–3385. https://doi.org/10.1093/nar/gkg520.

Shen, M., Sali, A., 2006. Statistical potential for assessment and prediction of protein structures. Protein Sci. 15, 2507–2524. https://doi.org/10.1110/ps.062416606.

Slonczewski, J.L., Fujisawa, M., Dopson, M., Krulwich, T.A., 2009. Cytoplasmic pH measurement and homeostasis in bacteria and archaea. Adv. Microb. Physiol. https://doi.org/10.1016/S0065-2911(09)05501-5.

Søndergaard, C.R., Garrett, A.E., Carstensen, T., Pollastri, G., Nielsen, J.E., 2009. Structural artifacts in protein-ligand X-ray structures: implications for the development of docking scoring functions. J. Med. Chem. 52, 5673–5684. https://doi.org/10.1021/jm8016464.

Steinbach, P.J., Brooks, B.R., 1994. New spherical-cutoff methods for long-range forces in macromolecular simulation. J. Comput. Chem. 15, 667–683. https://doi.org/10.1002/jcc.540150702.

Terashima, H., Kojima, S., Homma, M., 2008. Chapter 2 Flagellar Motility in Bacteria. Structure and Function of Flagellar Motor, International Review of Cell and Molecular Biology. Elsevier Inc., pp. 39–85

Terashima, H., Hirano, K., Inoue, Y., Tokano, T., Kawamoto, A., Kato, T., Yamaguchi, E., Namba, K., Uchihashi, T., Kojima, S., Homma, M., 2020. Assembly mechanism of a supramolecular MS-ring complex to initiate bacterial flagellar biogenesis in vibrio species. J. Bacteriol. 202, e00236-20. https://doi.org/10.1128/JB.00236-20.

Thomas, D.R., Morgan, D.G., DeRosier, D.J., 1999. Rotational symmetry of the C ring and a mechanism for the flagellar rotary motor. Proc. Natl. Acad. Sci. U.S.A. 96, 10134–10139. https://doi.org/10.1073/pnas.96.18.10134.

Thomas, D.R., Francis, N.R., Xu, C., DeRosier, D.J., 2006. The three-dimensional structure of the flagellar rotor from a clockwise-locked mutant of Salmonella enterica serovar typhimurium. J. Bacteriol. 188, 7039–7048. https://doi.org/10.1128/JB.00552-06.

Togashi, F., Yamaguchi, S., Kihara, M., Aizawa, S.I., Macnab, R.M., 1997. An extreme clockwise switch bias mutation in fliG of Salmonella typhimurium and its suppression by slow-motile mutations in motA and motB. J. Bacteriol. 179, 2994–3003. https://doi.org/10.1128/jb.179.9.2994-3003.1997.

Trabuco, L.G., Villa, E., Schreiner, E., Harrison, C.B., Schulten, K., 2009. Molecular dynamics flexible fitting: a practical guide to combine cryo-electron microscopy and X-ray crystallography. Methods 49, 174–180. https://doi.org/10.1016/j.ymeth.2009.04.005.

Waterhouse, A., Bertoni, M., Bienert, S., Studer, G., Tauriello, G., Gumienny, R., Heer, F.T., De Beer, T.A.P., Rempfer, C., Bordoli, L., Lepore, R., Schwede, T., 2018. SWISS-MODEL: homology modelling of protein structures and complexes. Nucleic Acids Res. 46, W296–W303. https://doi.org/10.1093/nar/gky427.

Webb, B., Sali, A., 2016. Comparative protein structure modeling using MODELLER. Curr. Protoc. Bioinforma. 15, 5.6.1–5.6.30. https://doi.org/10.1002/cpbi.3.

Xue, C., Lam, K.H., Zhang, H., Sun, K., Lee, S.H., Chen, X., Au, S.W.N., 2018. Crystal structure of the FliF-FliG complex from Helicobacter pylori yields insight into the assembly of the motor MS-C ring in the bacterial flagellum. J. Biol. Chem. 293, 2066–2078. https://doi.org/10.1074/jbc.M117.797936.